POLITECNICO DI TORINO
Repository ISTITUZIONALE

Assessing Uncertainty and Biases in Total Liquid Water Path Retrieved from W-, Ka-, and G-Band Radar/Radiometer Observations from Space

Original
Assessing Uncertainty and Biases in Total Liquid Water Path Retrieved from W-, Ka-, and G-Band Radar/Radiometer Observations from Space / Xu, Z., Kollias, P., Lebsock, M., Battaglia, A., Sasikumar, S.. - In: JOURNAL OF ATMOSPHERIC AND OCEANIC TECHNOLOGY. - ISSN 0739-0572. - 43:4(2026), pp. 373-387. [10.1175/jtech-d-25-0044.1]

Availability:
This version is available at: 11583/3009630 since: 2026-04-06T08:21:51Z

Publisher:
American Meteorological Society

Published
DOI:10.1175/jtech-d-25-0044.1

Terms of use:

This article is made available under terms and conditions as specified in the corresponding bibliographic description in the repository

Publisher copyright

(Article begins on next page)

09 October 2026

Assessing Uncertainty and Biases in Total Liquid Water Path Retrieved from W-, Ka-, and G-Band Radar/Radiometer Observations from Space

ZHUOCAN XU,[a] PAVLOS KOLLIAS,[a,b] MATTHEW LEBSOCK,[c] ALESSANDRO BATTAGLIA,[d,e] AND SUSMITHA SASIKUMAR[d]

[a] *Division of Atmospheric Sciences, Stony Brook University, State University of New York, Stony Brook, New York*
[b] *Department of Atmospheric and Oceanic Sciences, McGill University, Montreal, Quebec, Canada*
[c] *Jet Propulsion Laboratory, California Institute of Technology, Pasadena, California*
[d] *Department of Environment, Land and Infrastructure Engineering, Politecnico di Torino, Turin, Italy*
[e] *Department of Physics and Astronomy, University of Leicester, Leicester, United Kingdom*

(Manuscript received 20 April 2025, in final form 2 February 2026, accepted 19 February 2026)

ABSTRACT: Radar–radiometers that share the same antenna are of great interest due to their matched resolution and complementarity. Here, a spaceborne radar–radiometer simulator and high-resolution cloud model simulations are used to evaluate the impact of various sources of uncertainty and nonuniform beamfilling (NUBF) effects on the total liquid water path (TLWP) inferred from 238-, 94-, and 35.5-GHz brightness temperature (Tb) or path-integrated attenuation (PIA). Two maritime low cloud regimes are considered: drizzling stratocumulus (Sc) and trade wind shallow cumulus (Cu). Instrument precision, the sensitivity of observations to TLWP, and the natural variability of the relationship between the TLWP and the observable within forward simulations collectively determine the retrieval uncertainty of TLWP. Overall, TLWP retrievals are better constrained in Sc regimes due to their homogeneous appearance. The addition of 238-GHz PIA can be particularly advantageous for the Cu regime. A 50% or smaller retrieval uncertainty can be achieved starting at TLWP of 70 g m^{-2}, compared to more than 500 g m^{-2} by the 94-GHz PIA. In addition, instrument precision of Tb worse than 1 K can potentially escalate the uncertainties of TLWP. NUBF effects result in negative biases in observations and subsequent retrievals, the magnitude of which is commensurate with hydrometeor liquid amount and footprint size. Despite the biases in 238-GHz PIA caused by NUBF being the largest among the three frequencies considered, the associated error propagated into TLWP can be significantly lower than the other frequencies due to its high sensitivity.

KEYWORDS: Microwave observations; Radars/Radar observations; Satellite observations; Error analysis; Uncertainty

1. Introduction

Low-level clouds are widely distributed over the global oceans (Hartmann et al. 1992; Chi et al. 2024). Earth's radiation budget is highly sensitive to the properties of marine low clouds, while estimating their climate feedback with accurate sign and magnitude has been a long-standing challenge (Bony and Dufresne 2005; Sherwood et al. 2014). The contrast of low cloud feedback between stratocumulus and cumulus regimes in the Coupled Model Intercomparison Project phase 6 (CMIP6) remains largely muted compared to observations (Myers et al. 2021). In addition, CMIP6 found that the intermodel spread and multimodel mean in low cloud feedback further increased relative to CMIP5, due to a smaller increase of cloud liquid water path (CLWP) and more reduced cloud coverage responding to warming (Zelinka et al. 2020). Given radiative fluxes have a strong dependence on CLWP, a global map of CLWP that is solely attainable from satellite observations is essential to benchmark the performance of climate models.

One challenge with global CLWP datasets derived from passive solar or microwave imagers is that they differ significantly in the regional distributions (Seethala and Horváth, 2010). Observations from active sensors (lidar and radar) can resolve some of the discrepancy in passive datasets related to, among other factors, cloud occurrence, scattering geometry, cloud temperature, and precipitation occurrence (Lebsock and Su 2014; Greenwald et al. 2018), yet this understanding is not often reflected in the passive datasets used to evaluate models.

Another important cause of the differences in the CLWP estimates is the varying sensitivity of retrieval methods to cloud and rainwater, where microwave instruments are sensitive to both cloud and precipitation, while solar reflectance is primarily sensitive to cloud droplets. This difference can be exploited to simultaneously observe cloud and rainwater (Lebsock et al. 2011). The total liquid water path (TLWP) is defined as the column-integrated condensed water mass, comprising the sum of the CLWP and rain liquid water path (RLWP) components. The capability to observe cloud and precipitation simultaneously is vital to constrain microphysical processes (e.g., cloud-to-precipitation conversion) and improve their parameterizations in numerical models. Various synergistic combinations of W-band (frequency between 75 and 110 GHz) reflectivity with solar reflectances, microwave brightness temperatures (Tb), and radar path-integrated attenuation (PIA) as carried by the NASA A-train constellation have been used to constrain co-occurring cloud and rain (Lebsock et al. 2013; Mace et al. 2016) along with the associated model process

Denotes content that is immediately available upon publication as open access.

Corresponding author: Zhuocan Xu, zhuocan.xu@stonybrook.edu

DOI: 10.1175/JTECH-D-25-0044.1

© 2026 American Meteorological Society. This published article is licensed under the terms of the default AMS reuse license. For information regarding reuse of this content and general copyright information, consult the AMS Copyright Policy (www.ametsoc.org/PUBSReuseLicenses).

Unauthenticated | Downloaded 04/06/26 08:09 AM UTC

rates (Suzuki et al. 2013; Jing et al. 2019). Key to these studies is the exploitation of the sensitivity of solar reflection, microwave extinction/emission, and radar reflectivity to cloud, total, and rainwater, respectively. An optimal combination of the measurements requires that both cloud and rain be constrained simultaneously since all of the measurements have some sensitivity to both water modes (Xu et al. 2019).

This paper focuses on the use of radar-derived Tb and PIA measurements to constrain the TLWP, which provides a similar constraint to a passive microwave imager with two essential advantages: 1) The measurement is made on a spatial scale comparable to that of solar reflectance and 2) the radar reflectivity profile enables precise detection of precipitation occurrence. Existing efforts have used *CloudSat* (Stephens 2008) W-band PIA or Tb for this purpose. The presented study is very relevant to the Wind Velocity Radar Nephoscope (WIVERN) mission (Illingworth et al. 2018; Battaglia et al. 2022) that was recently selected as the European Space Agency (ESA) Earth Explorer 11 mission and included a radar–radiometer mode for improved Tb measurements. Combining additional frequencies, such as Ka (27–40 GHz) and G (110–300 GHz) bands, can add a significant amount of information to such underconstrained problems related to oceanic warm rain (Battaglia et al. 2014, 2020b; Courtier et al. 2024). The theoretical potential of G-band radar was established in the early 1990s (Lhermitte 1990) but not until recently has the maturity of technology enabled suborbital observations (Lamer et al. 2021; Courtier et al. 2022, 2024; Socuellamos et al. 2024) and consideration for satellite measurements.

This study has two primary objectives: first, to quantitatively estimate the TLWP uncertainties retrieved from Tb and PIA and their dependence on operating frequency and measurement uncertainty level. The analysis will provide a reference for future mission planning by mapping TLWP uncertainty requirements into observational uncertainty at each frequency; and second, to investigate how the nonuniform beamfilling (NUBF) effect biases the observations and translates into the derived TLWP and how these biases relate to observational frequency and instantaneous field of view (IFOV).

2. Background

a. Global LWP measurements

LWP climatologies have been primarily built upon passive microwave Tb or visible and near-IR imager observations (e.g., O'Dell et al. 2008; Elsaesser et al. 2017). Underpinned by different physical constraints, these methods are subject to their own uncertainty and bias mechanism. For microwave Tb, large errors can stem from the difficulties to partition the emission signals between cloud and precipitation as well as to determine the cloudy and clear-sky pixels accurately (Stephens and Kummerow 2007). For solar reflectances, LWP is derived from the retrievals of cloud effective radius and optical thickness using bispectral methods (Nakajima and King 1990). As such, uncertainties and biases in r_e and τ, associated with solar and viewing geometry, cloud inhomogeneity, plane-parallel assumption and precipitation occurrences, can populate into the LWP products (e.g., Marshak et al. 2006; Zhang et al. 2012; Xu et al. 2022).

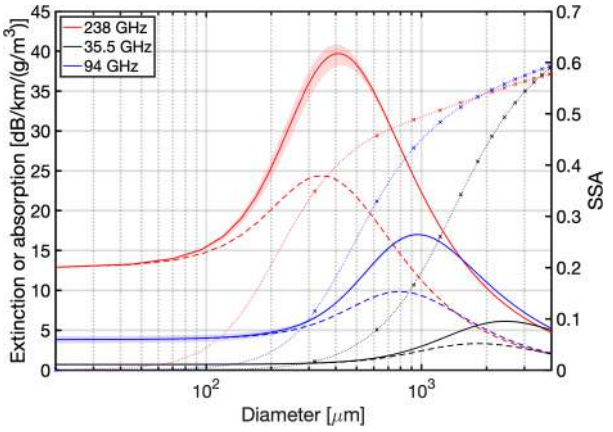

FIG. 1. Extinction (solid lines) and absorption coefficients (dash lines) per unit mass at 290 K. Red, blue, and black lines indicate 238, 94, and 35.5 GHz. Dotted lines with "x" markers indicate SSA. The shaded areas represent the variance of extinctions due to temperatures varying from 280 to 300 K.

Given the large discrepancies between Tb- and solar-reflectance-derived LWP and their dependence on cloud regimes, increasing efforts have been devoted to incorporating active sensors such as *CloudSat* and *CALIPSO* observations to validate and improve the LWP retrievals from space (Lebsock and Su 2014; Leinonen et al. 2016; Schulte et al. 2024). Leinonen et al. (2016) used the *CloudSat* PIA estimates to validate the CLWP retrievals in nonprecipitating clouds that combined *CloudSat* radar reflectivity and MODIS observations. The study pointed out a positive bias in the MODIS-derived CLWP, which likely results from the overestimation of cloud effective radius. More recently, Lebsock et al. (2022) used the *CloudSat* PIA to estimate the CLWP also in precipitation-free clouds. A comparison against the MODIS-based CLWP shows the increasing differences as CLWP increases. Note PIA (dB) is linearly proportional to CLWP without the presence of rain as in these two studies, while this relationship is no longer linear in the precipitating clouds.

b. Extinction and absorption at millimeter wavelengths

The wavelength-dependent radiative characteristics permit differential signals as a function of drop size. As illustrated in Fig. 1, scattering is negligible for drops below 50 μm for all the frequencies considered here. Extinction coefficients within this range show little dependence on size but increase commensurate with frequency. At 290 K, extinction per unit mass at 238 GHz for cloud size droplets exceeds 12 dB km^{-1}, while it is less than 1 dB km^{-1} at 35.5 GHz. The availability of G-band measurements is expected to enhance the detectability of cloud water, given its pronounced sensitivity to water mass. The extinction efficiency typically peaks around a size parameter of $2\pi r/\lambda \approx 1$, where r is the particle radius and λ is the radiation wavelength, for spherical particles in the Mie scattering regime, and single scattering albedo (SSA) increases monotonically. Due to the sensitivity of liquid water refractive index to temperature, extinction has a weak dependence on cloud

Unauthenticated | Downloaded 04/06/26 08:09 AM UTC

temperature, as indicated by the shaded areas in Fig. 1. The error in CLWP associated with cloud temperature at 94 GHz was found to be small (0.08%–2.24%) for nonraining clouds with tops lower than 2.5 km (Lebsock et al. 2022).

3. Methodology

Lebsock and Suzuki (2016) proposed a framework to evaluate how measurement and forward model uncertainties propagate into TLWP derived from 94-GHz Tb and PIA for trade wind cumulus (Cu). They underscored the dominant impact of NUBF and the natural variability in the relationship between observables and TLWP. Here, we extend that assessment to include 35- and 238-GHz channels as well and consider two predominant and climatically important low cloud regimes: Cu and open-cell stratocumulus (Sc) with drizzle.

Tb and PIA, as integral constraints on LWP, are demonstrated to be of great value even in the multifrequency radar observing systems (Xu et al. 2019; Battaglia et al. 2020a). PIA (always intended as a two-way attenuation) is readily available from radars with uncertainties notably smaller over the ocean relative to land. PIA due to hydrometeors is defined as

$$\mathrm{PIA} = -10\log_{10}^{(e^{-2\tau})}, \tag{1}$$

where τ denotes the path-integrated extinction of cloud and rain droplets. The physical basis to retrieve LWP from PIA is that cloud extinction is linearly correlated with cloud water mass for a given temperature, although the occurrence of precipitation introduces ambiguities.

The surface reference technique (SRT; Nakamura 1991; Lebsock and L'Ecuyer 2011) is often adopted to estimate PIA. The SRT estimates the PIA by subtracting the normalized radar backscatter cross section of the surface (σ_o) in cloudy regions from the clear-sky σ_o measured within close proximity:

$$\mathrm{PIA} = \sigma_{o,\mathrm{clear}} - \sigma_{o,\mathrm{cloudy}}. \tag{2}$$

Gaseous attenuation exists in both clear-sky and cloudy regions and thus is canceled out in Eq. (2). It is temperature and frequency dependent and can exceed 5.5 dB (two way) in the tropics for a W band (Haynes et al. 2009) and be even more pronounced at G band. The impact of atmospheric gases on σ_o must be considered. Taking $\sigma_{o,\mathrm{clear}}$ as a baseline, the presence of clouds and precipitation results in a measurable depression from the baseline.

Passive microwave Tb can be acquired with independent radiometers or from radars in radiometric mode, as experimented in the *CloudSat* mission. The *CloudSat* Tb is perfectly collocated with reflectivity observations, although its measurement uncertainty (~4 K with radar integration length of 1.1 km) is much higher than that of stand-alone radiometers (≤1 K). Observed Tb represents a column-integrated signal that includes upward emission from hydrometeors and water vapor, scattering by ice particles and large raindrops, gaseous absorption, and surface emissivity. To isolate the contribution

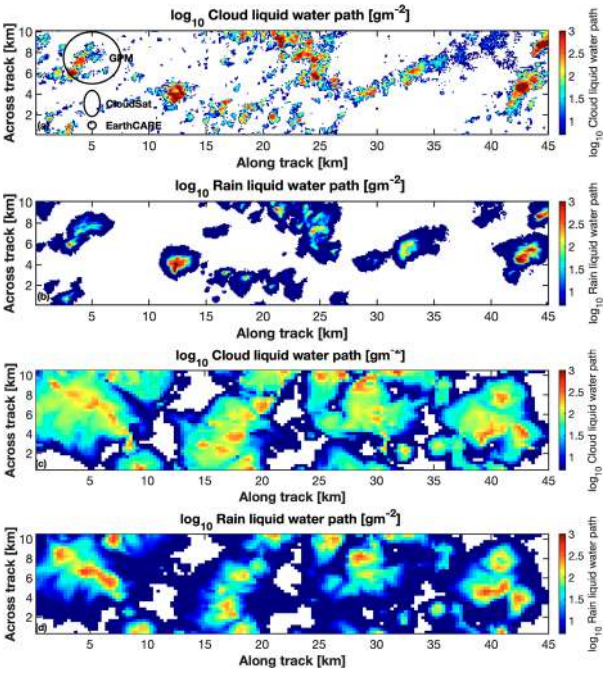

FIG. 2. Examples of simulated (a) CLWP and (b) RLWP on log base 10 scale for shallow Cu scene at native model resolution. IFOV of GPM, *CloudSat,* and *EarthCARE* are provided in (a) for reference. (c),(d), As in (a) and (b), but for Sc scene.

of cloud and precipitation to the signal, ΔT_b can be estimated analogously to SRT for PIA:

$$\Delta T_b = T_{b,\mathrm{cloudy}} - T_{b,\mathrm{clr}}. \tag{3}$$

Here, $T_{b,\mathrm{cloudy}}$ and $T_{b,\mathrm{clr}}$ represent the brightness temperatures measured over the cloudy column and the nearby clear region, respectively.

Following Battaglia et al. (2020a), a radar simulator is coupled to numerical model outputs to map the cloud and rain microphysics at the fine model grid scale to what radars and radiometers with different footprints would observe. Nadir-view Tb and hydrometeor extinction are first computed at the model's native resolution and then convolved with a two-dimensional Gaussian antenna gain pattern with varying 3-dB beamwidths. The footprint radius is perturbed from 0.1 to 2 km to evaluate the NUBF effects. Further details are provided in section 3b.

Simulations of Cu and Sc are produced using different cloud models. Despite variations in model setup, both simulations are representative of the target cloud scenes at sufficiently fine resolutions. As shown in Fig. 2, Cu clouds are organized in small clusters with generally larger CLWP relative to Sc, consistent with observations in nature. The cloud properties of Cu can vary significantly within 1 km, making them challenging to observe with GPM and even *CloudSat* (Fig. 2a). The cloud variability at scales smaller than the radar footprint is smoothed and challenging to resolve due to the NUBF effect. *Earth Cloud, Aerosol, and Radiation Explorer* (*EarthCARE*) radar, with an IFOV of 700 m, is anticipated to

Unauthenticated | Downloaded 04/06/26 08:09 AM UTC

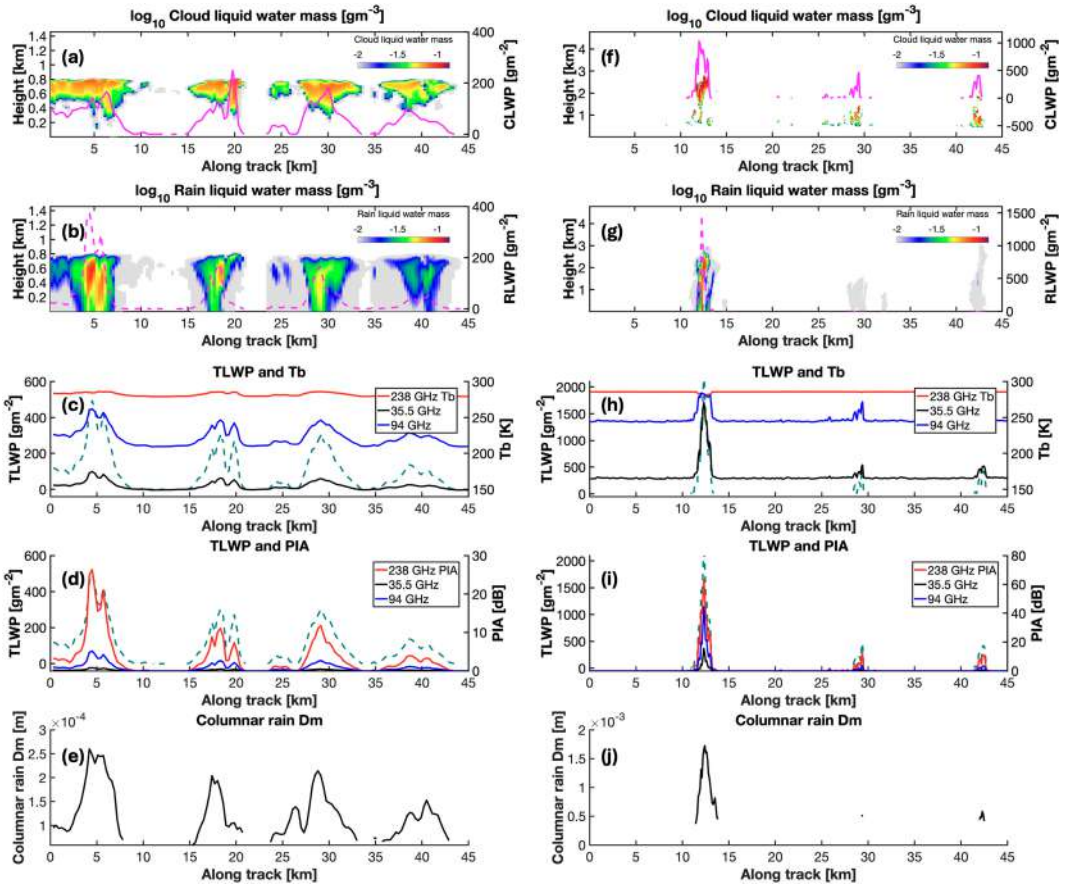

FIG. 3. An example period of (a) cloud and (b) rain liquid water content from the Sc simulations at model resolutions. Solid and dash lines in magenta indicate CLWP and RLWP, respectively. (c) The 238-, 94-, and 35.5-GHz forward computed Tbs. (d) Forward computed PIA at the same frequencies. In (c) and (d), the dash lines in teal represent TLWP. (e) Columnar rain D_m. (f)–(j) As in (a)–(e), but for Cu scene simulations.

provide new insights into Cu from space. In contrast, drizzling Sc exhibits smaller LWP variance, with most profiles containing TLWP less than 500 g m^{-2}. Their broader horizontal extent is also a key factor in mitigating biases caused by NUBF.

Figure 3 presents an example cross section of microphysics and forward-simulated Tb and PIA at model resolution from the Sc scene. PIA is strongly correlated with TLWP, with 238 GHz showing the highest sensitivity. The clear-sky Tb increases with frequency; at 238 GHz, it exceeds 270 K, leaving a narrow margin for an enhanced emission signal in regions containing hydrometeors.

a. Cloud model simulations

The shallow cumulus field was simulated based on observations from the Rain in Cumulus over the Ocean (RICO) field campaign, which was conducted around the islands of Antigua and Barbuda from December 2004 to January 2005. The primary goals of RICO were to investigate how precipitation forms in shallow cumulus clouds and how it affects both individual cumuli and the broader cloud field (Rauber et al. 2007). Simulations for the present study were produced using the System for Atmospheric Modeling (SAM; Khairoutdinov and Randall 2003), with a two-moment Morrison microphysics scheme (Morrison et al. 2005). An exponential distribution was assumed for the rain drop size distributions (DSDs) with the intercept parameter (N_{0r}) set to be 8×10^6 m^{-4} (Marshall and Palmer 1948). The size of the domain was $57.6 \times 57.6 \times 4.8$ km^3, with horizontal and vertical model resolutions fixed at 100 and 40 m, respectively.

For the Sc regime, large-eddy simulations were generated using the Distributed Hydrodynamic Aerosol and Radiative Modeling Application (DHARMA) model (Ackerman et al. 2004; Zhou et al. 2018). The initial wind and thermodynamic profiles were composited from measurements during the second research flight of DYCOMS II (Stevens et al. 2003). The domain size was $60 \times 60 \times 1.5$ km^3. The horizontal grid spacing is 300 m, which is slightly coarser than the RICO simulations but significantly smaller than the footprints of most spaceborne radars. The difference in horizontal resolution between Sc and Cu simulations may affect the results, though the impact is considered small, as a relatively coarser resolution is sufficient to capture the variability of Sc. The vertical grid spacing was height dependent to allow for finer resolution near the surface. The microphysics scheme used was a

Unauthenticated | Downloaded 04/06/26 08:09 AM UTC

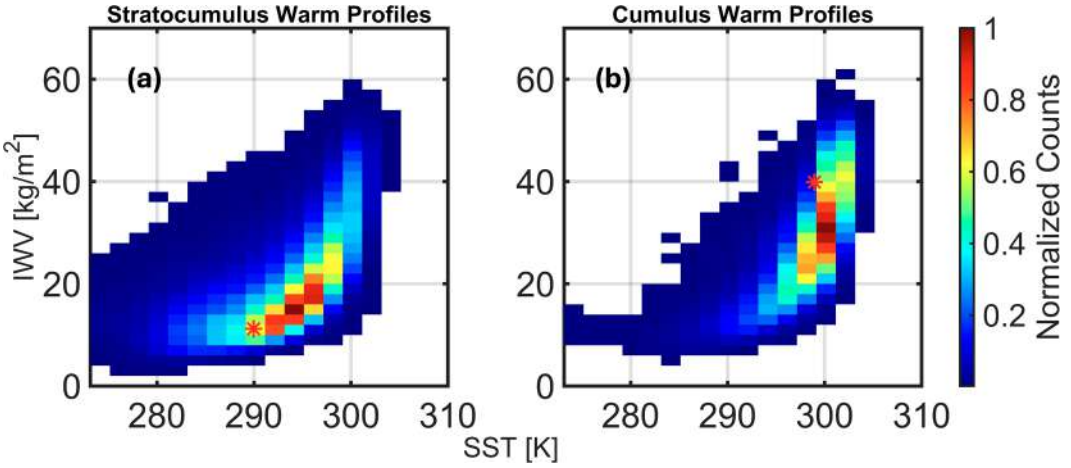

FIG. 4. (a) The frequency distribution of single-layer Sc as a function of SST and IWV determined from a year of *CloudSat*, *CALIPSO*, and coincident reanalysis data. (b) As in (a), but for Cu. The red asterisks indicate the median of SST and IWV for the two cloud model simulation datasets adopted in this study.

modified version of the two-moment Morrison scheme, adapted to improve representations of supersaturation and cloud droplet activation (Morrison and Grabowski 2008), consistent with the original focus on cloud–aerosol interactions in Zhou et al. (2018). Cloud droplet number concentration was prescribed at 10 cm^{-3}, which is within the characteristic range of open-cell Sc observed over the southeast Pacific Ocean (Wood et al. 2011). A gamma distribution was assumed for the rain DSDs with the shape parameter fixed at 3 (Testud et al. 2001).

The 32-h simulation included a spinup period of approximately 3 h, after which the cloud field reached a quasi-steady state. The temporal evolution of domain-averaged LWP (~60 g m^{-2}), cloud cover (~0.5), and surface precipitation (~1 mm day^{-1}) remained minimal. Hence, simulations at 16.5 and 24 h are used for the current study.

Cu and Sc occur in distinct environments characterized by a broad spectrum of sea surface temperature (SST) and integrated water vapor (IWV). Using a year of *CloudSat*, *CALIPSO*, and reanalysis data (2B-CLDCLASS-LIDAR, 2C-PRECIP-COLUMN, and ECMWF-AUX), the frequency distributions of SST and IWV conditions in Sc and Cu regimes are estimated (Fig. 4). Cu formation is more favored in warmer and more humid conditions. The red asterisks in the figure indicate the median SST and IWV values from the cloud model simulations used in this study. These model datasets are representative of a subset of maritime low clouds frequently observed in nature. Accordingly, while the magnitudes inferred from our error analysis are specific to the simulations used, the broader conclusions are expected to hold more generally.

b. Radiation forward model

The scattering and extinction properties of cloud and raindrops are computed using Mie theory (Bohren and Huffman 1983). The model proposed by Ellison (2007) is used to calculate the complex refractive index of water. Gaseous absorption is treated with the model from Rosenkranz (1998). Microwave brightness temperatures are computed using the two-stream Eddington approximation (Kummerow 1993). Surface reflection is treated with the Fresnel model for the ocean surface. The salinity is set to be constant at 35 g kg^{-1}. The normalized backscatter cross section at surface is estimated as a function of SST and 10-m wind speed according to Wu (1990).

4. Results

a. TLWP retrieval uncertainties

The uncertainties of TLWP (σ_{TLWP}) inferred from Tb or PIA are modulated by several factors, including instrument precisions (σ_{T_b} and σ_{PIA}), the sensitivity of the observation to TLWP (S_{T_b} and S_{PIA}), and the natural variabilities in the relationships between the forward simulated observations and TLWP. The natural variability in the clear-sky pixels, denoted by $\delta_{T_{b,\mathrm{clear}}}$ and $\delta_{\mathrm{PIA}_{\mathrm{clear}}}$, can be influenced by columnar water vapor, SSTs, and surface winds. In addition, the variability in cloudy regions (δ_{T_b} and δ_{PIA}) is subject to hydrometeor DSDs and their vertical profiles. Together with sensitivity, these three sources of uncertainty are propagated to estimate σ_{TLWP} via the following formulations as in Lebsock and Suzuki (2016), where the subscript freq indicates the operating frequency:

$$\sigma_{\mathrm{TLWP,freq}} = \frac{\sqrt{\sigma^2_{T_b} + \delta^2_{T_{b,\mathrm{clear,freq}}} + \delta^2_{T_{b,\mathrm{freq}}}}}{S_{T_b,\mathrm{freq}}}, \tag{4}$$

$$\sigma_{\mathrm{TLWP,freq}} = \frac{\sqrt{\sigma^2_{\mathrm{PIA}} + \delta^2_{\mathrm{PIA}_{\mathrm{clear}},\mathrm{freq}} + \delta^2_{\mathrm{PIA,freq}}}}{S_{\mathrm{PIA,freq}}}. \tag{5}$$

Lebsock and Suzuki provided an estimation for σ_{TLWP} retrieved from the 94-GHz Tb or PIA using large-eddy simulations based on the RICO dataset. In this study, we extend the quantitative analysis to include σ_{TLWP} estimates inferred from 35- and 238-GHz observations and consider two marine low cloud regimes: Cu and Sc. The σ_{TLWP} is assessed assuming retrievals from a single-frequency Tb or PIA. The S_{T_b} and S_{PIA}

Unauthenticated | Downloaded 04/06/26 08:09 AM UTC

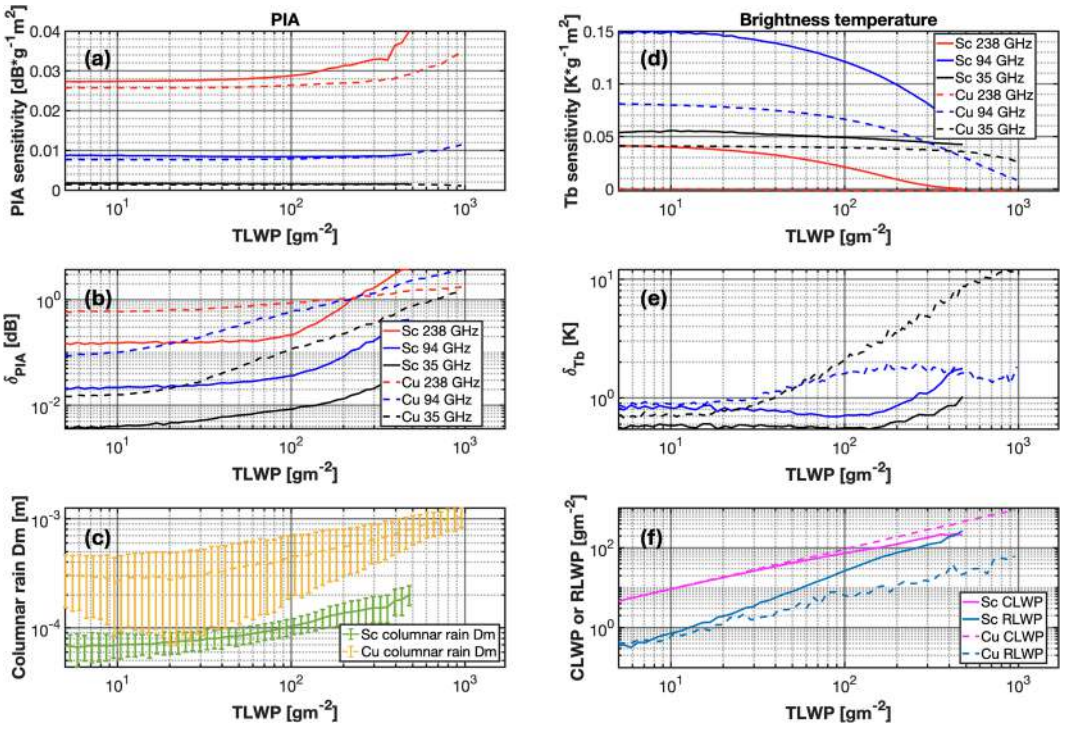

FIG. 5. (a) The sensitivity of PIA calculated with a 20 g m^{-2} perturbation of the TLWP. (b) The δ_{PIA} for a given TLWP. Red, blue, and black lines indicate 238, 94, and 35 GHz, respectively. See legends for cloud types. (d),(e) As in (a) and (b), but for the Tb. (c) The median and standard deviations of columnar rain Dm for a given TLWP. (f) The median of CLWP and RLWP for a given TLWP.

are calculated using a finite-difference approximation with a perturbation of 20 g m^{-2} TLWP.

Figures 5a, 5b, 5d, and 5e show the various terms contributing to Eqs. (4) and (5) as a function of TLWP. Instrument precision does not vary with TLWP, whereas natural variability and the sensitivity of PIA and Tb to TLWP depend on the operating frequency and the TLWP magnitude. As such, δ_{T_b}, δ_{PIA}, S_{T_b}, and S_{PIA} of each frequency are displayed as a function of TLWP that is binned logarithmically (Fig. 5). The S_{T_b} and S_{PIA} are calculated as the medians of data points within every bin, while δ_{T_b} and δ_{PIA} are calculated as the standard deviations within each bin. The $\delta_{T_{b,\mathrm{clear}}}$ and $\delta_{\mathrm{PIA}_{\mathrm{clear}}}$ are estimated by first calculating the standard deviations of clear-sky Tb (PIA) within ±25 km of a cloudy profile and then taking the median of every TLWP bin.

The detailed information of the columnar rain Dm, CLWP, and RLWP are displayed in Figs. 5c and 5f, respectively, as hydrometeor DSDs that are largely affected by rain occurrences are also a key factor in regulating the sensitivity of observation to TLWP. The columnar rain Dm provides a characteristic size estimation for the entire column, which is defined as the total of rain Dm weighted by the corresponding rainwater mass at each cloudy level in the column.

We first focus on the sensitivity of the observations to changes in TLWP. As shown in Fig. 5a, S_{PIA} increases with frequency monotonically. Provided the same TLWP of 20 g m^{-2}, PIA for the Sc scene at 35, 94, and 238 GHz is 0.04, 0.17, and 0.55 dB, respectively. When TLWP is small and CLWP dominates, S_{PIA} is practically invariant with TLWP, governed by the linear dependence of extinction on cloud mass content. The small difference regarding S_{PIA} between Sc and Cu is likely caused by the different cloud temperatures. As TLWP and RLWP increase, $S_{\mathrm{PIA},238}$ is the first to rise due to the fact that at G band, drops with radius larger than 100 μm are already almost a factor of 2 more efficient than small droplets in extinguishing radiation (Fig. 1). The growth of $S_{\mathrm{PIA},238}$ accelerates with the presence of bigger raindrops (Fig. 5c) that results in amplified extinction. The disparity of $S_{\mathrm{PIA},238}$ between Sc and Cu increases with increasing TLWP, which can be associated with the growing contribution of rain component for Sc while RLWP remaining about 10% of TLWP for Cu (Fig. 5f).

In contrast to S_{PIA}, S_{T_b} tends to decrease with the increasing TLWP, as T_b values are prone to saturation with the growing LWP. Higher-frequency T_b values are more susceptible to gaseous emission (primarily water vapor, Table 1) and to higher ocean nadir emissivities. As a result, the baseline T_b values where clouds and precipitation are absent increase with frequency (Fig. 3c), leading to a reduced dynamical range of T_b values when moving from clear to heavy precipitation. As evident in Fig. 5d, the clear-sky $T_{b,238}$ for tropical Cu (red dash line) is already too warm to allow for any sensitivity to hydrometeors. Therefore, $T_{b,238}$ affords basically no constraints for low-level liquid clouds in the tropics, though it can be informative in colder and drier environments. For that reason,

Unauthenticated | Downloaded 04/06/26 08:09 AM UTC

TABLE 1. The median and interquartile range (IQR) of two-way water vapor attenuation (dB) in cloudy and clear sky of Cu and Sc model simulations.

	238-GHz median/IQR	94-GHz median/IQR	35-GHz median/IQR
Cloudy (Cu)	27.5/0.97	4.0/0.14	0.89/0.024
Clear (Cu)	26.67/0.82	3.9/0.12	0.87/0.021
Cloudy (Sc)	8.3/0.27	1.22/0.039	0.29/0.007
Clear (Sc)	8.0/0.17	1.19/0.025	0.28/0.004

further quantitative estimations are omitted for $T_{b,238}$ in this study. Similarly, the distinctions of S_{T_b} at the same frequency between subtropical Sc and tropical Cu are mainly attributable to environmental humidity (thus of different baseline levels). For instance, clear-sky $T_{b,94}$ for Sc is around 212 K, while clear-sky $T_{b,94}$ for Cu is 245 K on average (Fig. 3h), implying the diminished dynamical range for Cu. Also noticeable is the significant decline of $S_{T_b,94}$ when TLWP is in excess of 100 g m^{-2}, whereas $S_{T_b,35}$ sustains. It verifies the superiority of $T_{b,35}$, when the target shifts to the regime dominated by the rain size drops.

We now consider the natural variability in the relationships between the observables and the TLWP. The higher-frequency δ_{PIA} is consistently more pronounced than the lower-frequency δ_{PIA} below the TLWP of 200 g m^{-2} for the same cloud scene (Fig. 5b). Occasionally, this frequency dependence can be reversed when Dm is in the range of maximum extinction efficiency for a lower frequency (e.g., Fig. 1). This effect can be seen in Fig. 5b comparing $\delta_{\mathrm{PIA},94}$ (blue dash line) and $\delta_{\mathrm{PIA},238}$ (red dash line), as columnar rain Dm grows to ~600 μm (Fig. 5c). Also note that for Cu, the ratio between CLWP and RLWP is consistently ~9:1 regardless of the TLWP amount, whereas the fraction of water in the rain mode increases as TLWP increases for the Sc case (Fig. 5f). The variations of $\delta_{\mathrm{PIA},94}$ and $\delta_{\mathrm{PIA},35}$ with TLWP appears to strongly covary with columnar rain Dm. The large-size raindrops associated with higher standard deviations within bins are indicative of more variable and broader DSDs with increasing TLWP in Cu, giving rise to greater δ_{PIA} and δ_{T_b} relative to Sc.

We now turn to evaluate the impact of measurement accuracy on the TLWP retrieval uncertainties via perturbations (e.g., Zhao et al. 2014). The measurement accuracy is perturbed from 0.25 to 4 K and from 0.1 to 0.3 dB for Tb and PIA, respectively. For reference, *CloudSat* CPR has a 0.16-dB precision for PIA and 4-K precision for Tb. Since *CloudSat* utilized the radar noise to generate an experimental product of Tb, it sets an upper bound for Tb measurement accuracy. Independent radiometers and future radar systems are expected to have better accuracy.

Across all three frequencies, relative σ_{TLWP} tends to decrease with larger TLWP (Figs. 6 and 7). In comparison with Cu, Sc appears to be better constrained from a single-frequency Tb or PIA due to its overall smaller natural variability and higher observational sensitivity to TLWP. For instance, σ_{TLWP} is <15% in Sc and above 60% in Cu at the same TLWP of 200 g m^{-2} using 94-GHz PIA provided the identical instrument accuracy of 0.1 dB (red lines in Figs. 6b,e). In addition, higher-frequency observation outperforms the counterpart at lower frequency. For shallow cumulus in particular, the availability of G-band PIA would substantially improve the retrievals of TLWP, permitting the inference of TLWP with 50% uncertainty down to 70 g m^{-2} (vs 525 g m^{-2} with W-band PIA, Table 2, Figs. 6a,b). Considering a retrieval target at 50%, the 94-GHz Tb can outmatch the 238-GHz PIA in Cu, if both are provided with their optimal accuracy (Table 2).

However, it is worth noting that the constraints from Tb are contingent on instrument accuracy for the range tested. There is a significantly wider spread of σ_{TLWP} between the lowest (purple lines in Figs. 6 and 7) and highest (red lines in Figs. 6 and 7) instrument precision in Tb-based relative to PIA-based retrievals, implying that the instrument error of Tb can have a more important role in driving σ_{TLWP}. Increasing Tb precision from 0.25 to 2 K induces a jump of relative σ_{TLWP} at 35 g m^{-2} TLWP from 50% to 90% (Fig. 7a). At a given TLWP, the change in σ_{TLWP} with instrument precision increasing from 0.25 to 1 K is relatively small and becomes more substantial as the precision exceeds 1 K.

As exemplified in Fig. 5d, S_{T_b} can be strongly dependent on the environmental conditions, and the degree of such dependence increases with frequency. Combining the *CloudSat*, *CALIPSO*, and reanalysis data (2B-CLDCLASS-LIDAR, 2C-PRECIP-COLUMN, and ECMWF-AUX), an estimation on global scale is provided regarding how S_{T_b} within the cumulus regime varies with IWV and SST (Fig. 8). The S_{T_b} is primarily a function of IWV and presents a secondary dependence on SST, though evidently the two factors covary. As moving toward the tropics, the Tb sensitivity to TLWP is dampened at all three frequencies. The S_{T_b} at 238 GHz is most susceptible to the transition of environment, declining from a maximum of 0.35 in cold and dry atmosphere to very small values in humid and warm environment (Fig. 8a). The $T_{b,238}$ has larger sensitivity than $T_{b,94}$ where IWV is <10 kg m^{-2} (asterisks in Fig. 8a). In addition, S_{T_b} decreases as TLWP increases. The loss of sensitivity with growing TLWP is also more pronounced at higher frequencies. At TLWP of 100 g m^{-2}, $T_{b,94}$ would offer the optimal constraints among the three frequencies considered, given its superior sensitivity in almost all environmental conditions.

b. *Biases due to NUBF effects*

NUBF effects are potentially one of the major sources of biases in spaceborne remote sensing retrievals (Durden 2018; Short et al. 2015; among others), the magnitude of which depends on instrument footprint size, operating frequency, and the cloud heterogeneity within the IFOV. NUBF biases emanate from the fact that the relationships between observations and geophysical variables are nonlinear and often cloud and precipitation only partially fill the footprint. Given the impact of NUBF appears nearly negligible for the Sc simulations considered, the discussion here will be focused on the Cu regime.

As proposed in Battaglia et al. (2020a), the "true" PIA and the observed SRT-based PIA that is subject to the NUBF effect can be expressed as follows:

Unauthenticated | Downloaded 04/06/26 08:09 AM UTC

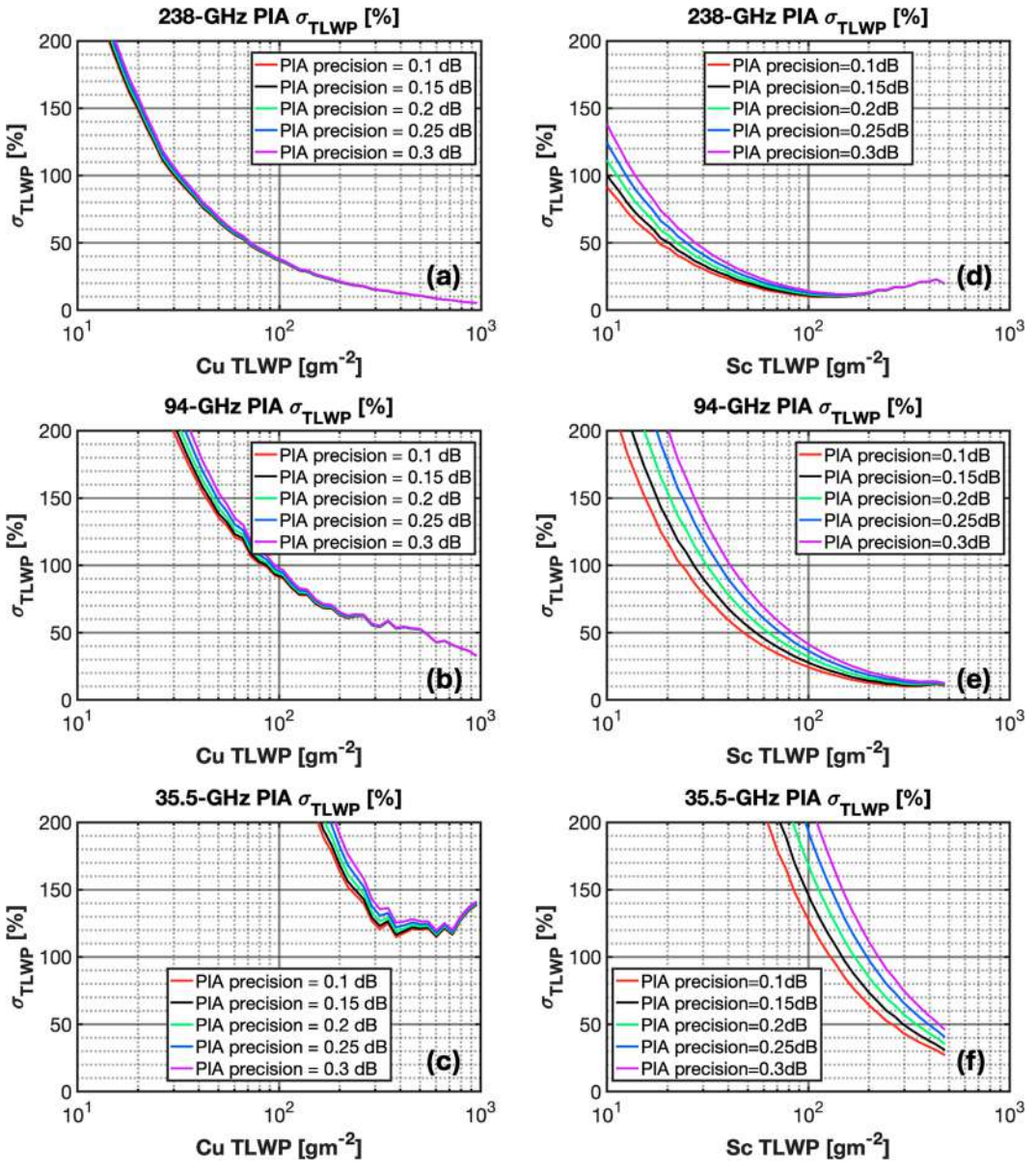

FIG. 6. Relative uncertainties of TLWP in Cu retrieved from PIA at (a) 238, (b) 94, and (c) 35 GHz. (d)–(f) As in (a)–(c), but for Sc. Relative σ_{TLWP} is defined as σ_{TLWP} scaled by TLWP in percentage.

$$\mathrm{PIA}_{\text{“true”}} \equiv \frac{\iint_{\Omega} G^2(\hat{\Omega})\mathrm{pia}(\hat{\Omega})d\Omega}{\iint_{\Omega} G^2(\hat{\Omega})d\Omega}, \tag{6}$$

$$\mathrm{PIA}_{\mathrm{SRT}} \equiv 10\log_{10}^{\left\{\iint_{\Omega} G^2(\hat{\Omega})\exp[-\mathrm{pia}(\hat{\Omega})/4.343]d\Omega / \iint_{\Omega} G^2(\hat{\Omega})d\Omega\right\}}, \tag{7}$$

where G indicates the two-way antenna gain and Ω indicates the direction within the footprint to integrate. The $\mathrm{PIA}_{\mathrm{SRT}}$ is consistently smaller than $\mathrm{PIA}_{\mathrm{true}}$, unless hydrometeor properties are homogeneous and $\mathrm{pia}(\hat{\Omega})$ do not vary within the IFOV.

Results are shown in Figs. 9 and 10. As displayed in Fig. 9, the biases due to NUBF are already evident at 1-km footprint across all the frequencies considered for the RICO-like cumulus. The 1 km is slightly smaller than the footprint of *CloudSat* CPR, and we expect less NUBF for the EarthCARE CPR with its footprint of 0.7 km. The biases in PIA are always negative with magnitude increasingly more pronounced at higher frequency. Also revealed is the reduced range of $\mathrm{PIA}_{\mathrm{SRT}}$ relative to $\mathrm{PIA}_{\mathrm{true}}$, as a consequence of the underfootprint-scale cloud variability being smoothed out.

The biases are further examined as a function of footprint-averaged TLWP ($\overline{\mathrm{TLWP}}$), which is computed by convolving model-resolution TLWP with one-way antenna gain function.

Unauthenticated | Downloaded 04/06/26 08:09 AM UTC

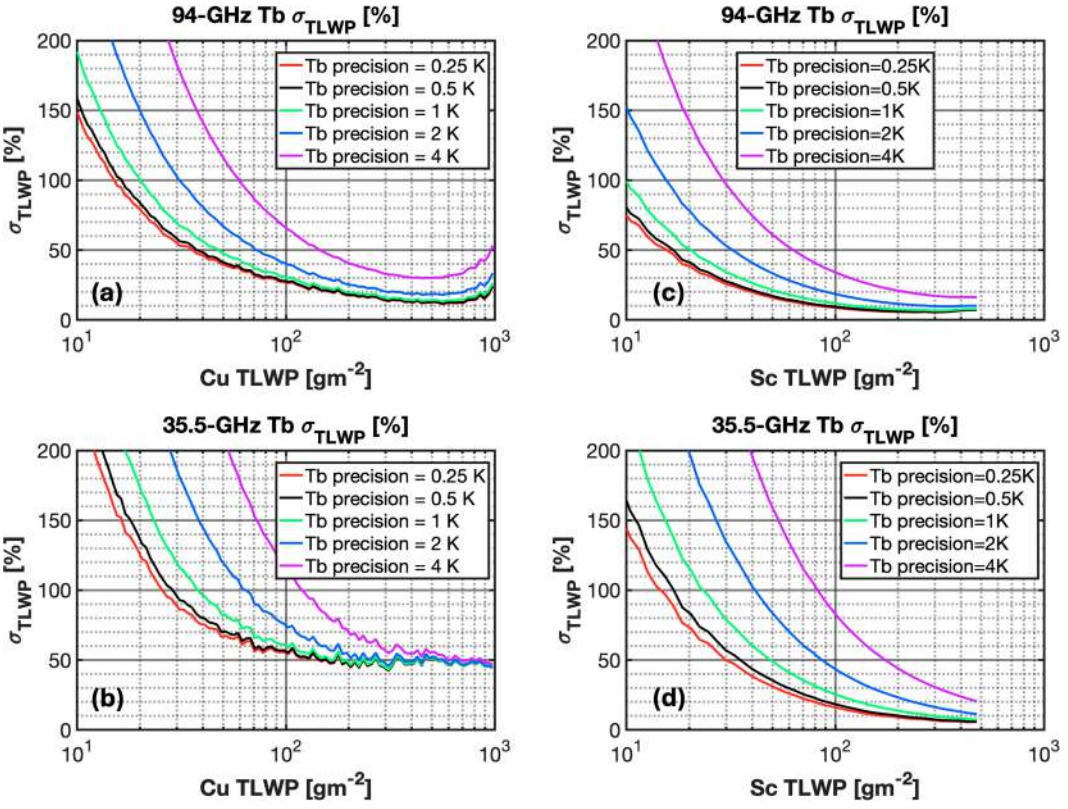

FIG. 7. As in Fig. 6, but for 94- and 35-GHz Tbs.

Figures 10a–c present the median difference between PIA_{true} and PIA_{SRT} within each bin of $\overline{TLWP}$. The radius of the footprint is perturbed from 0.1 to 2 km. The biases are commensurate with footprint size and also monotonically increase with $\overline{TLWP}$. The bias of 238-GHz PIA at 400 g m^{-2} is about −13 dB, whereas that bias at 35.5 GHz is less than −2 dB. Nevertheless, the frequency dependence of the magnitude of the NUBF effect on the derived $\overline{TLWP}$ reverses when their differing sensitivity is taken into account. Specifically, in Figs. 10d–f, the sensitivity of PIA to TLWP (Fig. 5a) is used to propagate the NUBF error in observation to retrievals. The fact that G band is far more sensitive than Ka band results in the maximum biases in relative error of TLWP is about −120% at G band and reaches −250% at Ka band. It is emphasized the advantage that the G band can bring in terms of deriving TLWP from radar observations.

As for brightness temperature, Tb_{true} is computed by first convolving the hydrometeor extinction with the Gaussian antenna gain function and then conducting the radiative transfer calculations of Tb. The observed Tb that is under NUBF effect is obtained by averaging the model-resolution Tb with antenna gain. Similar to PIA, NUBF causes Tb and consequently retrieved TLWP biased low. A causal factor that differentiates the behavior of Tb from PIA is the tendency of higher-frequency Tb to become saturated and thus less sensitive with increasing TLWP. The 35.5-GHz sensitivity exceeds that of 94 GHz around TLWP of 400 g m^{-2} (Fig. 5d). The saturation of $T_{b,94}$ is also reflected in Fig. 11. Tb biases due to NUBF are less significant at lower frequency when $\overline{TLWP}$ is small (e.g., <250 g m^{-2}). As $\overline{TLWP}$ continues to grow, 94-GHz Tb biases approach an asymptote, whereas 35.5-GHz biases keep rising. The aforementioned factors also confound the NUBF effect translated into the retrieved TLWP. The contrast of Tb-derived TLWP error between W and Ka band (Figs. 11c,d) is much less dramatic than the PIA-based TLWP error (Figs. 10e,f).

TABLE 2. The minimum TLWP (g m^{-2}) where relative uncertainties σ_{TLWP} meet a target of 50% provided the optimal instrument accuracy (0.1 dB for PIA and 0.25 K for Tb).

	238 GHz	94 GHz	35 GHz
Tb (Cu)	—	35	150
PIA (Cu)	70	525	—
Tb (Sc)	—	17	30
PIA (Sc)	20	48	260

5. Summary

Spaceborne radar reflectivity observations are essential for advancing our understanding of low-level marine clouds and their associated precipitation. However, these observations often provide incomplete vertical profiles of cumulus (Cu) and stratocumulus (Sc) clouds due to limited radar sensitivity, surface clutter contamination, and the shallow vertical extent of such clouds (Burns et al. 2016; Lamer et al. 2020).

Unauthenticated | Downloaded 04/06/26 08:09 AM UTC

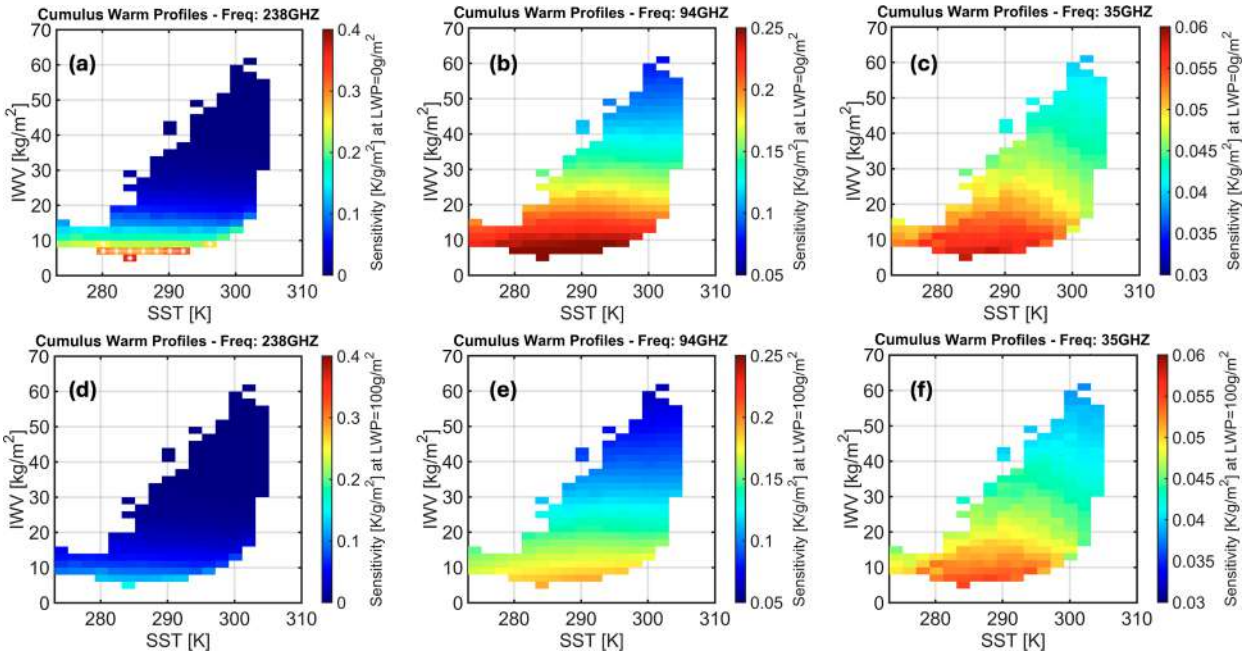

FIG. 8. (a)–(c) The frequency distribution of 238-, 94-, and 35-GHz Tb sensitivity estimated at TLWP = 0 g m^{-2} in single-layer Cu observed by *CloudSat* and *CALIPSO* as a function of SST and IWV. White markers in (a) represent where 238-GHz Tb is more sensitive than 94-GHz Tb. (d)–(f) As in (a)–(c), but at TLWP = 100 g m^{-2}.

To better characterize the aerosol–cloud–precipitation interactions in these cloud systems, coincident estimates of total liquid water path (TLWP) derived from path-integrated attenuation (PIA) and brightness temperature (Tb) measurements are needed. These estimates must be obtained with high sensitivity—to capture the full range of TLWP values—and at high spatial resolution to mitigate nonuniform beamfilling (NUBF) effects. NUBF can introduce substantial biases in TLWP retrievals, particularly for Cu clouds, which exhibit small-scale spatial variability that is poorly resolved by the large footprints of traditional microwave radiometers.

In this study, we consider future spaceborne radar systems, such as NASA's Atmosphere Observing System (AOS; Vane et al. 2022), that include in the radar design a dedicated radiometric mode that will enable the measurement of the Tb corresponding to the same antenna field of view, with sufficient accuracy to improve on the PIA estimate. The performance of Tb and PIA measurements at the same frequency, conducted by a radar–radiometer system at three different radar bands: G-, W-, and Ka band, is investigated here. A comprehensive radar–radiometer simulator and high-resolution cloud resolving model simulations are used to quantitatively assess how the retrieval uncertainty of TLWP in Cu and Sc is modulated by the instrument accuracy level, the sensitivity of Tb or PIA to TLWP, and the natural variability in relationships between forward calculated observations and TLWP. The instrument accuracy of Tb and PIA is, respectively, perturbed from 0.25 to 4 K and from 0.1 to 0.3 dB to demonstrate the impact of precisions. Individual experiments were conducted for 238-, 94-, and 35.5-GHz Tb and PIA. In addition, the high resolution of cloud model outputs allows the evaluation of the biases introduced by

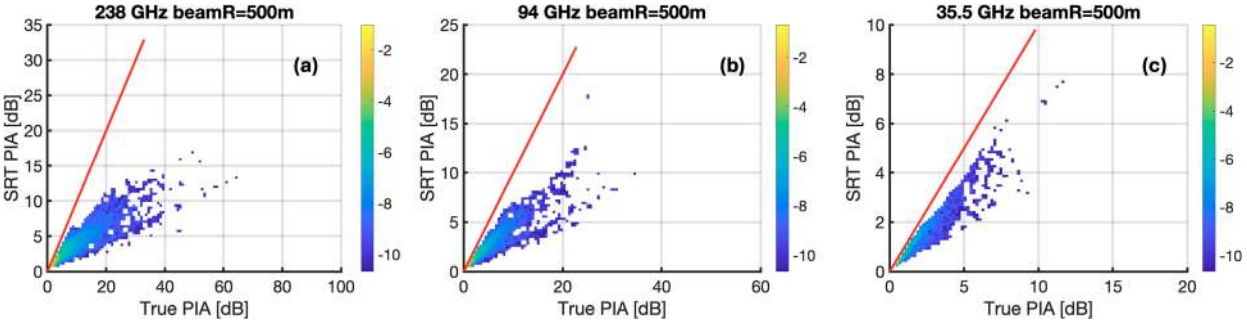

FIG. 9. Density plot of SRT PIA vs true PIA at 3-dB footprint of 1 km with all the Cu simulations for (a) 238, (b) 94, and (c) 35.5 GHz. Red lines indicate the 1-to-1 line to manifest the biases. The beamR is the footprint radius.

Unauthenticated | Downloaded 04/06/26 08:09 AM UTC

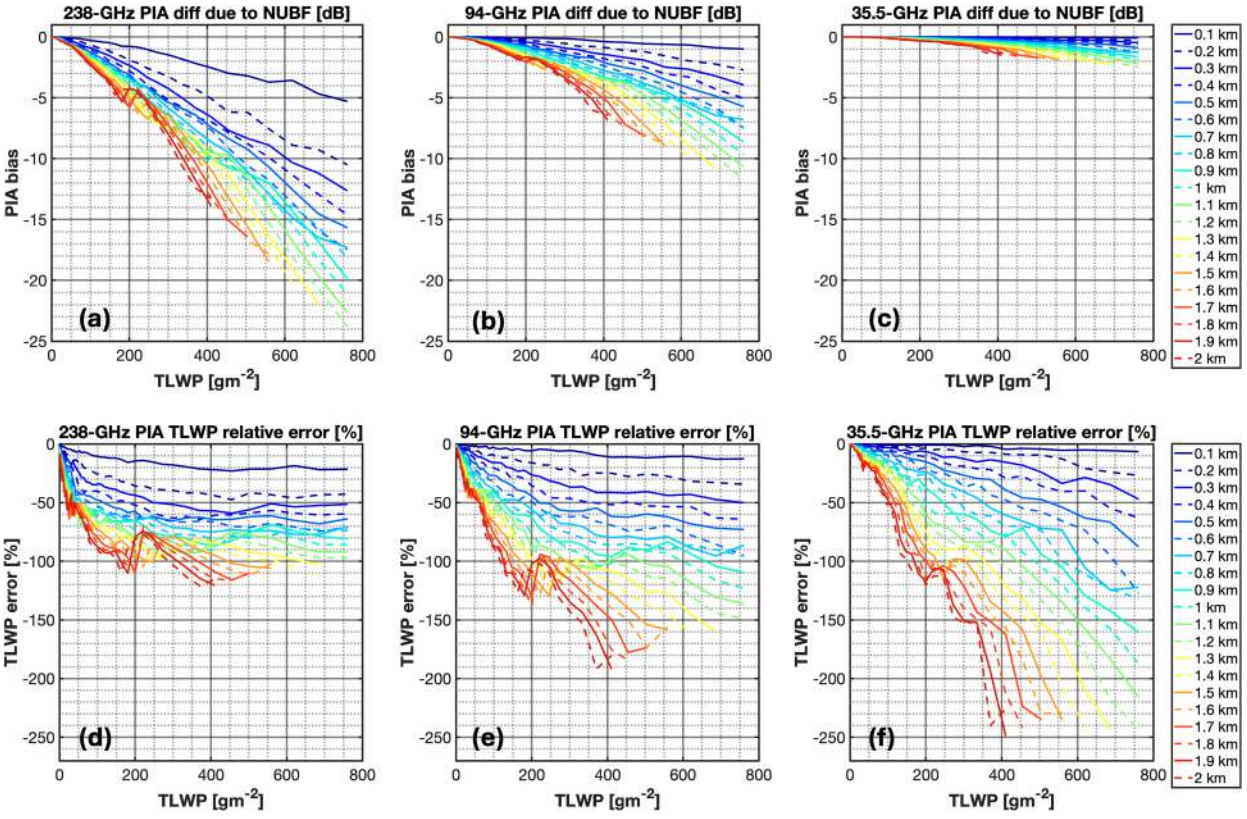

FIG. 10. The bin median of PIA biases as a function of footprint averaged TLWP for (a) 238, (b) 94, and (c) 35.5 GHz. Colors indicate the radius of 3-dB footprint as specified in legend. Bins with less than 200 samples are omitted. (d)–(f) As in (a)–(c), but for relative error of retrieved TLWP in percentage.

NUBF effects at different footprint sizes. The main findings are as follows:

- The availability of G-band PIA could extend the capability of detecting smaller TLWP and significantly reduces the TLWP retrieval uncertainties, particularly for Cu. The PIA sensitivity to TLWP increases by a factor of 3 at 238 GHz compared to 94 GHz. For example, for a TLWP of 40 g m^{-2}, the PIA at 94 and 238 GHz is estimated to be <0.4 and >1 dB, respectively. Considering that the uncertainty in the estimation of the PIA for *CloudSat* is ~0.7 dB, this suggests that such small TLWP amounts are only detectable by the 238-GHz PIA. Moreover, a target retrieval uncertainty of TLWP at 50% can be achieved with 238-GHz PIA at TLWP as small as 70 g m^{-2}.
- The sensitivity of the Tb values to TLWP is the result of the interplay between two factors: 1) how cold is the baseline clear-sky Tb which is colder at lower frequencies and in drier, colder environments and 2) the extinction coefficient of liquid particles per unit mass, which increases with frequency. Overall, the 94-GHz Tb exhibits the highest sensitivity to TLWP for most Cu and Sc clouds across the full range of temperature and humidity conditions in which these clouds typically form. The sensitivity of 238-GHz Tb surpasses that of 94 GHz only in very dry and cold environments—specifically, where integrated water vapor is less than 10 kg m^{-2}. In contrast, 35-GHz Tb becomes useful primarily in conditions with large amounts of LWP and precipitation.
- In terms of TLWP retrievals, drizzling stratocumulus clouds appear to be better constrained than cumulus clouds, as a result of both their overall lower variability in drop size distribution (DSD) and the greater sensitivity of observations to TLWP.
- The increase in TLWP retrieval uncertainties due to the deterioration of instrument accuracy varies significantly with TLWP for Tb-based retrievals (Fig. 7), whereas its dependence on TLWP for PIA-based retrievals is minimal. This implies that instrument precision is more critical for Tb-based retrievals than for PIA-based retrievals, particularly at low TLWP values.
- NUBF effects lead to negative biases in PIA, Tb, and consequently in the retrieved TLWP. These biases tend to increase with both footprint size and TLWP. It is important to note that a large bias in the observation does not necessarily translate into a large bias in the retrieval. In the case of the Cu regime, NUBF can induce biases in 238-GHz PIA that are up to 8 times greater than those at 35 GHz. Nevertheless, the corresponding biases in TLWP are largely mitigated by the high sensitivity of the 238-GHz channel, resulting in comparable—or even smaller—biases in the retrieved TLWP. When compared to PIA at the same frequency, NUBF-induced biases in Tb appear to be better contained for TLWP values exceeding 100 g m^{-2}.

Unauthenticated | Downloaded 04/06/26 08:09 AM UTC

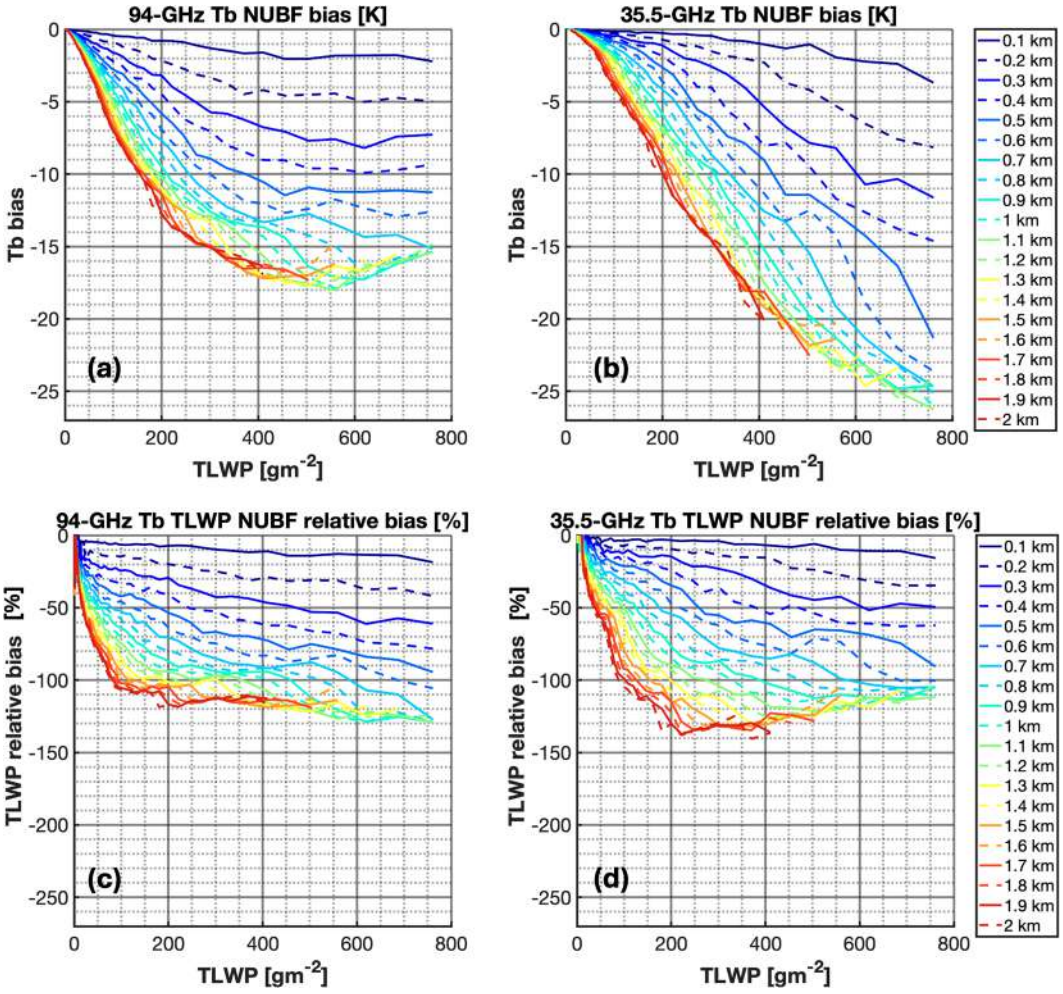

FIG. 11. As in Figs. 10b, 10c, 10e, and 10f, but for Tb.

Optimal retrievals will employ a multifrequency approach that leverages both PIA and Tb measurements. This strategy exploits the strengths of each observation type, including their regime-dependent sensitivity, uncertainty characteristics, and dynamic range. Retrievals that combine multifrequency observations are also better equipped to capture the underlying hydrometeor DSDs, thereby improving the partitioning between coexisting cloud and precipitation.

Finally, we consider the impact of the presented work in current and planned spaceborne radar missions. The recently launched *Earth Cloud, Aerosol, and Radiation Explorer* (*EarthCARE*) satellite mission features a highly sensitive 94-GHz radar with enhanced low-level detection and Doppler capability (Illingworth et al. 2015; Kollias et al. 2014, 2022). While the Doppler measurements are expected to improve the detection of precipitation size particles, the *EarthCARE* Cloud Profiling Radar (CPR) will still face limitations in characterizing the TLWP.

The newly selected Wind Velocity Radar Nephoscope (WIVERN) mission, part of the European Space Agency (ESA) Earth Explorer 11 program, takes this a step further by incorporating a radar–radiometer mode into a 94-GHz conically scanning Doppler radar system (Illingworth et al. 2018). With a 500-MHz receiver bandwidth and a 3-m antenna dish, the WIVERN mission is expected to provide 94-GHz Tbs at a 600-m footprint resolution and with better than 0.5-K measurement accuracy. Together, the WIVERN and EarthCARE missions will provide spaceborne W-band radar observations for at least the next 15 years.

The present analysis further suggests that even a well-designed radar–radiometer system—such as that implemented on WIVERN—may not be sufficient to achieve accurate TLWP retrievals across the full dynamic range of atmospheric conditions. A logical next step would be to complement the W-band observations with a G-band radar–radiometer system operating in formation with these ESA Earth Explorer missions. Due to its short wavelength and low peak power transmitters available at this frequency, the G-band radar radiometer will have a small size, weight, and power (SWaP) footprint and thus offer an attractive, cost-effective technology to deploy in space. This dual-frequency configuration would offer the benefits of complementary PIA and Tb measurements at two frequencies, as

Unauthenticated | Downloaded 04/06/26 08:09 AM UTC

well as differential signals from hydrometeor layers (Socuellamos et al. 2024; Lamer et al. 2021; Battaglia and Panegrossi 2020; Xu et al. 2019).

Acknowledgments. This research has been supported by the European Space Agency (ESA) under the RAINCAST project Contract Continuation Notice 2 (ESA Contract ESA AO/1-9324/18/NL/NA) and the National Aeronautics and Space Administration (NASA) under the Atmospheric Observing System (AOS) project (Contract 80NSSC23M0113). The work of Matthew Lebsock was performed at the Jet Propulsion Laboratory, California Institute of Technology, under a contract with the National Aeronautics and Space Administration (Contract 80NM0018D0004).

Data availability statement. 2B-CLDCLASS-LIDAR (R05) that combines *CloudSat* CPR and *CALIPSO* lidar measurements is available at https://www.cloudsat.cira.colostate.edu/data-products/2b-cldclass-lidar. 2C-PRECIP-COLUMN (R05) is available at https://www.cloudsat.cira.colostate.edu/data-products/2c-precip-column. Reanalysis data are available at https://www.cloudsat.cira.colostate.edu/data-products/ecmwf-aux. Model data are available upon request.

REFERENCES

Ackerman, A. S., M. P. Kirkpatrick, D. E. Stevens, and O. B. Toon, 2004: The impact of humidity above stratiform clouds on indirect aerosol climate forcing. *Nature*, **432**, 1014–1017, https://doi.org/10.1038/nature03174.

Battaglia, A., and G. Panegrossi, 2020: What can we learn from the CloudSat radiometric mode observations of snowfall over the ice-free ocean? *Remote Sens.*, **12**, 3285, https://doi.org/10.3390/rs12203285.

——, C. D. Westbrook, S. Kneifel, P. Kollias, N. Humpage, U. Löhnert, J. Tyynelä, and G. W. Petty, 2014: G band atmospheric radars: New frontiers in cloud physics. *Atmos. Meas. Tech.*, **7**, 1527–1546, https://doi.org/10.5194/amt-7-1527-2014.

——, P. Kollias, R. Dhillon, K. Lamer, M. Khairoutdinov, and D. Watters, 2020a: Mind the gap—Part 2: Improving quantitative estimates of cloud and rain water path in oceanic warm rain using spaceborne radars. *Atmos. Meas. Tech.*, **13**, 4865–4883, https://doi.org/10.5194/amt-13-4865-2020.

——, and Coauthors, 2020b: Spaceborne cloud and precipitation radars: Status, challenges, and ways forward. *Rev. Geophys.*, **58**, e2019RG000686, https://doi.org/10.1029/2019RG000686.

——, P. Martire, E. Caubet, L. Phalippou, F. Stesina, P. Kollias, and A. Illingworth, 2022: Observation error analysis for the WInd VElocity Radar Nephoscope W-band Doppler conically scanning spaceborne radar via end-to-end simulations. *Atmos. Meas. Tech.*, **15**, 3011–3030, https://doi.org/10.5194/amt-15-3011-2022.

Bohren, C. F., and D. R. Huffman, 1983: *Absorption and Scattering of Light by Small Particles.* Wiley, 530 pp.

Bony, S., and J.-L. Dufresne, 2005: Marine boundary layer clouds at the heart of tropical cloud feedback uncertainties in climate models. *Geophys. Res. Lett.*, **32**, L20806, https://doi.org/10.1029/2005GL023851.

Burns, D., P. Kollias, A. Tatarevic, A. Battaglia, and S. Tanelli, 2016: The performance of the EarthCARE cloud profiling radar in marine stratiform clouds. *J. Geophys. Res. Atmos.*, **121**, 14 525–14 537, https://doi.org/10.1002/2016JD025090.

Chi, Y., C. Zhao, Y. Yang, X. Zhao, and J. Yang, 2024: Global characteristics of cloud macro-physical properties from active satellite remote sensing. *Atmos. Res.*, **302**, 107316, https://doi.org/10.1016/j.atmosres.2024.107316.

Courtier, B. M., and Coauthors, 2022: First observations of G-band radar Doppler spectra. *Geophys. Res. Lett.*, **49**, e2021GL096475, https://doi.org/10.1029/2021GL096475.

——, A. Battaglia, and K. Mroz, 2024: Advantages of G-band radar in multi-frequency, liquid phase microphysical retrievals. *Atmos. Meas. Tech.*, **17**, 6875–6888, https://doi.org/10.5194/amt-17-6875-2024.

Durden, S. L., 2018: Relating GPM radar reflectivity profile characteristics to path-integrated attenuation. *IEEE Trans. Geosci. Remote Sens.*, **56**, 4065–4074, https://doi.org/10.1109/TGRS.2018.2821601.

Ellison, W. J., 2007: Permittivity of pure water, at standard atmospheric pressure, over the frequency range −25 THz and the temperature range −100°C. *J. Phys. Chem. Ref. Data*, **36**, 1–18, https://doi.org/10.1063/1.2360986.

Elsaesser, G. S., C. W. O'Dell, M. D. Lebsock, R. Bennartz, T. J. Greenwald, and F. J. Wentz, 2017: The Multisensor Advanced Climatology of Liquid Water Path (MAC-LWP). *J. Climate*, **30**, 10 193–10 210, https://doi.org/10.1175/jcli-d-16-0902.1.

Greenwald, T. J., R. Bennartz, M. Lebsock, and J. Teixeira, 2018: An uncertainty data set for passive microwave satellite observations of warm cloud liquid water path. *J. Geophys. Res. Atmos.*, **123**, 3668–3687, https://doi.org/10.1002/2017JD027638.

Hartmann, D. L., M. E. Ockert-Bell, and M. L. Michelsen, 1992: The effect of cloud type on Earth's energy balance: Global analysis. *J. Climate*, **5**, 1281–1304, https://doi.org/10.1175/1520-0442(1992)005<1281:TEOCTO>2.0.CO;2.

Haynes, J. M., T. S. L'Ecuyer, G. L. Stephens, S. D. Miller, C. Mitrescu, N. B. Wood, and S. Tanelli, 2009: Rainfall retrieval over the ocean with spaceborne W-band radar. *J. Geophys. Res.*, **114**, D00A22, https://doi.org/10.1029/2008JD009973.

Illingworth, A. J., and Coauthors, 2015: The EarthCARE satellite: The next step forward in global measurements of clouds, aerosols, precipitation, and radiation. *Bull. Amer. Meteor. Soc.*, **96**, 1311–1332, https://doi.org/10.1175/BAMS-D-12-00227.1.

——, and Coauthors, 2018: WIVERN: A new satellite concept to provide global in-cloud winds, precipitation, and cloud properties. *Bull. Amer. Meteor. Soc.*, **99**, 1669–1687, https://doi.org/10.1175/BAMS-D-16-0047.1.

Jing, X., K. Suzuki, and T. Michibata, 2019: The key role of warm rain parameterization in determining the aerosol indirect effect in a global climate model. *J. Climate*, **32**, 4409–4430, https://doi.org/10.1175/JCLI-D-18-0789.1.

Khairoutdinov, M. F., and D. A. Randall, 2003: Cloud resolving modeling of the ARM summer 1997 IOP: Model formulation, results, uncertainties, and sensitivities. *J. Atmos. Sci.*, **60**, 607–625, https://doi.org/10.1175/1520-0469(2003)060<0607:CRMOTA>2.0.CO;2.

Kollias, P., S. Tanelli, A. Battaglia, and A. Tatarevic, 2014: Evaluation of EarthCARE cloud profiling radar Doppler velocity measurements in particle sedimentation regimes. *J. Atmos. Oceanic Technol.*, **31**, 366–386, https://doi.org/10.1175/JTECH-D-11-00202.1.

——, A. Battaglia, K. Lamer, B. P. Treserras, and S. A. Braun, 2022: Mind the gap—Part 3: Doppler velocity measurements from space. *Front. Remote Sens.*, **3**, 860284, https://doi.org/10.3389/frsen.2022.860284.

Unauthenticated | Downloaded 04/06/26 08:09 AM UTC

Kummerow, C., 1993: On the accuracy of the Eddington approximation for radiative transfer in the microwave frequencies. *J. Geophys. Res.*, **98**, 2757–2765, https://doi.org/10.1029/92JD02472.

Lamer, K., P. Kollias, A. Battaglia, and S. Preval, 2020: Mind the gap—Part 1: Accurately locating warm marine boundary layer clouds and precipitation using spaceborne radars. *Atmos. Meas. Tech.*, **13**, 2363–2379, https://doi.org/10.5194/amt-13-2363-2020.

——, M. Oue, A. Battaglia, R. J. Roy, K. B. Cooper, R. Dhillon, and P. Kollias, 2021: Multifrequency radar observations of clouds and precipitation including the G-band, *Atmos. Meas. Tech.*, **14**, 3615–3629, https://doi.org/10.5194/amt-14-3615-2021.

Lebsock, M. D., and T. S. L'Ecuyer, 2011: The retrieval of warm rain from CloudSat. *J. Geophys. Res.*, **116**, D20209, https://doi.org/10.1029/2011JD016076.

——, and H. Su, 2014: Application of active spaceborne remote sensing for understanding biases between passive cloud water path retrievals. *J. Geophys. Res. Atmos.*, **119**, 8962–8979, https://doi.org/10.1002/2014JD021568.

——, and K. Suzuki, 2016: Uncertainty characteristics of total water path retrievals in shallow cumulus derived from spaceborne radar/radiometer integral constraints. *J. Atmos. Oceanic Technol.*, **33**, 1597–1609, https://doi.org/10.1175/JTECH-D-16-0023.1.

——, T. S. L'Ecuyer, and G. L. Stephens, 2011: Detecting the ratio of rain and cloud water in low-latitude shallow marine clouds. *J. Appl. Meteor. Climatol.*, **50**, 419–432, https://doi.org/10.1175/2010JAMC2494.1.

——, H. Morrison, and A. Gettelman, 2013: Microphysical implications of cloud-precipitation covariance derived from satellite remote sensing. *J. Geophys. Res. Atmos.*, **118**, 6521–6533, https://doi.org/10.1002/jgrd.50347.

——, H. Takahashi, R. Roy, M. J. Kurowski, and L. Oreopoulos, 2022: Understanding errors in cloud liquid water path retrievals derived from *CloudSat* path-integrated attenuation. *J. Appl. Meteor. Climatol.*, **61**, 955–967, https://doi.org/10.1175/JAMC-D-21-0235.1.

Leinonen, J., M. D. Lebsock, G. L. Stephens, and K. Suzuki, 2016: Improved retrieval of cloud liquid water from *CloudSat* and MODIS. *J. Appl. Meteor. Climatol.*, **55**, 1831–1844, https://doi.org/10.1175/JAMC-D-16-0077.1.

Lhermitte, R., 1990: Attenuation and scattering of millimeter wavelength radiation by clouds and precipitation. *J. Atmos. Oceanic Technol.*, **7**, 464–479, https://doi.org/10.1175/1520-0426(1990)007<0464:AASOMW>2.0.CO;2.

Mace, G. G., S. Avey, S. Cooper, M. Lebsock, S. Tanelli, and G. Dobrowalski, 2016: Retrieving co-occurring cloud and precipitation properties of warm marine boundary layer clouds with A-train data. *J. Geophys. Res. Atmos.*, **121**, 4008–4033, https://doi.org/10.1002/2015JD023681.

Marshak, A., S. Platnick, T. Várnai, G. Wen, and R. F. Cahalan, 2006: Impact of three-dimensional radiative effects on satellite retrievals of cloud droplet sizes. *J. Geophys. Res.*, **111**, D09207, https://doi.org/10.1029/2005JD006686.

Marshall, J. S., and W. M. Palmer, 1948: The distribution of raindrops with size. *J. Meteor.*, **5**, 165–166, https://doi.org/10.1175/1520-0469(1948)005<0165:TDORWS>2.0.CO;2.

Morrison, H., and W. W. Grabowski, 2008: Modeling supersaturation and subgrid-scale mixing with two-moment bulk warm microphysics. *J. Atmos. Sci.*, **65**, 792–812, https://doi.org/10.1175/2007JAS2374.1.

——, J. A. Curry, and V. I. Khvorostyanov, 2005: A new double-moment microphysics parameterization for application in cloud and climate models. Part I: Description. *J. Atmos. Sci.*, **62**, 1665–1677, https://doi.org/10.1175/JAS3446.1.

Myers, T. A., R. C. Scott, M. D. Zelinka, S. A. Klein, J. R. Norris, and P. M. Caldwell, 2021: Observational constraints on low cloud feedback reduce uncertainty of climate sensitivity. *Nat. Climate Change*, **11**, 501–507, https://doi.org/10.1038/s41558-021-01039-0.

Nakajima, T., and M. King, 1990: Determination of the optical thickness and effective particle radius of clouds from reflected solar radiation measurements. Part I: Theory. *J. Atmos. Sci.*, **47**, 1878–1893, https://doi.org/10.1175/1520-0469(1990)047<1878:DOTOTA>2.0.CO;2.

Nakamura, K., 1991: Biases of rain retrieval algorithms for spaceborne radar caused by nonuniformity of rain. *J. Atmos. Oceanic Technol.*, **8**, 363–373, https://doi.org/10.1175/1520-0426(1991)008<0363:BORRAF>2.0.CO;2.

O'Dell, C. W., F. J. Wentz, and R. Bennartz, 2008: Cloud liquid water path from satellite-based passive microwave observations: A new climatology over the global oceans. *J. Climate*, **21**, 1721–1739, https://doi.org/10.1175/2007JCLI1958.1.

Rauber, R. M., and Coauthors, 2007: Rain in shallow cumulus over the ocean: The RICO campaign. *Bull. Amer. Meteor. Soc.*, **88**, 1912–1928, https://doi.org/10.1175/BAMS-88-12-1912.

Rosenkranz, P. W., 1998: Water vapor microwave continuum absorption: A comparison of measurements and models. *Radio Sci.*, **33**, 919–928, https://doi.org/10.1029/98RS01182.

Schulte, R. M., M. D. Lebsock, J. M. Haynes, and Y. Hu, 2024: A random forest algorithm for the prediction of cloud liquid water content from combined CloudSat–CALIPSO observations. *Atmos. Meas. Tech.*, **17**, 3583–3596, https://doi.org/10.5194/amt-17-3583-2024.

Seethala, C., and A. Horváth, 2010: Global assessment of AMSR-E and MODIS cloud liquid water path retrievals in warm oceanic clouds. *J. Geophys. Res.*, **115**, D13202, https://doi.org/10.1029/2009JD012662.

Sherwood, S., C. Sandrine Bony, and J.-L. Dufresne, 2014: Spread in model climate sensitivity traced to atmospheric convective mixing. *Nature*, **505**, 37–42, https://doi.org/10.1038/nature12829.

Short, D. A., R. Meneghini, A. E. Emory, and M. R. Schwaller, 2015: Reduction of nonuniform beamfilling effects by multiple constraints: A simulation study. *J. Atmos. Oceanic Technol.*, **32**, 2114–2124, https://doi.org/10.1175/JTECH-D-15-0021.1.

Socuellamos, J. M., R. Rodriguez Monje, M. D. Lebsock, K. B. Cooper, and P. Kollias, 2024: Dual-frequency (Ka-band and G-band) radar estimates of liquid water content profiles in shallow clouds. *Atmos. Meas. Tech.*, **17**, 6965–6981, https://doi.org/10.5194/egusphere-2024-2090.

Stephens, G. L., and C. D. Kummerow, 2007: The remote sensing of clouds and precipitation from space: A review. *J. Atmos. Sci.*, **64**, 3742–3765, https://doi.org/10.1175/2006JAS2375.1.

——, and Coauthors, 2008: CloudSat mission: Performance and early science after the first year of operation. *J. Geophys. Res.*, **113**, D00A18, https://doi.org/10.1029/2008JD009982.

Stevens, B., and Coauthors, 2003: Dynamics and Chemistry of Marine Stratocumulus—DYCOMS II. *Bull. Amer. Meteor. Soc.*, **84**, 579–593, https://doi.org/10.1175/BAMS-84-5-579.

Suzuki, K., J.-C. Golaz, and G. L. Stephens, 2013: Evaluating cloud tuning in a climate model with satellite observations. *Geophys. Res. Lett.*, **40**, 4464–4468, https://doi.org/10.1002/grl.50874.

Unauthenticated | Downloaded 04/06/26 08:09 AM UTC

Testud, J., S. Oury, R. A. Black, P. Amayenc, and X. Dou, 2001: The concept of "normalized" distribution to describe raindrop spectra: A tool for cloud physics and cloud remote sensing. *J. Appl. Meteor.*, **40**, 1118–1140, https://doi.org/10.1175/1520-0450(2001)040<1118:TCONDT>2.0.CO;2.

Vane, D., and Coauthors, 2022: The Atmosphere Observing System (AOS): A core component of NASA's Earth System Observatory (ESO). *2022 IEEE Aerospace Conf. (AERO)*, Big Sky, MT, Institute of Electrical and Electronics Engineers, 1–7, https://doi.org/10.1109/AERO53065.2022.9843507.

Wood, R., C. S. Bretherton, D. Leon, A. D. Clarke, P. Zuidema, G. Allen, and H. Coe, 2011: An aircraft case study of the spatial transition from closed to open mesoscale cellular convection over the southeast Pacific. *Atmos. Chem. Phys.*, **11**, 2341–2370, https://doi.org/10.5194/acp-11-2341-2011.

Wu, J., 1990: Mean square slopes of the wind-disturbed water surface, their magnitude, directionality, and composition. *Radio Sci.*, **25**, 37–48, https://doi.org/10.1029/RS025i001p00037.

Xu, Z., G. G. Mace, and D. J. Posselt, 2019: A method for assessing relative skill in retrieving cloud and precipitation properties in next-generation cloud radar and radiometer orbiting observatories. *J. Atmos. Oceanic Technol.*, **36**, 2283–2306, https://doi.org/10.1175/JTECH-D-18-0204.1.

——, ——, and ——, 2022: Impact of rain on retrieved warm cloud properties using visible and near-infrared reflectances using Markov Chain Monte Carlo techniques. *IEEE Trans. Geosci. Remote Sens.*, **60**, 4110110, https://doi.org/10.1109/TGRS.2022.3208007.

Zelinka, M. D., T. A. Myers, D. T. McCoy, S. Po-Chedley, P. M. Caldwell, P. Ceppi, S. A. Klein, and K. E. Taylor, 2020: Causes of higher climate sensitivity in CMIP6 models. *Geophys. Res. Lett.*, **47**, e2019GL085782, https://doi.org/10.1029/2019GL085782.

Zhang, Z., A. S. Ackerman, G. Feingold, S. Platnick, R. Pincus, and H. Xue, 2012: Effects of cloud horizontal inhomogeneity and drizzle on remote sensing of cloud droplet effective radius: Case studies based on large-eddy simulations. *J. Geophys. Res.*, **117**, D19208, https://doi.org/10.1029/2012JD017655.

Zhao, C., S. Xie, X. Chen, M. P. Jensen, and M. Dunn, 2014: Quantifying uncertainties of cloud microphysical property retrievals with a perturbation method. *J. Geophys. Res. Atmos.*, **119**, 5375–5385, https://doi.org/10.1002/2013JD021112.

Zhou, X., A. S. Ackerman, A. M. Fridlind, and P. Kollias, 2018: Simulation of mesoscale cellular convection in marine stratocumulus. Part I: Drizzling conditions. *J. Atmos. Sci.*, **75**, 257–274, https://doi.org/10.1175/JAS-D-17-0070.1.

Unauthenticated | Downloaded 04/06/26 08:09 AM UTC